3-2021

Particle-in-Cell Simulation of an Industrial Magnetron with Electron Population Analysis

Andong Yue
Boise State University

Marcus Pearlman
Boise State University

Mike Worthington
L3Harris Technologies, Inc.

John Cipolla
L3Harris Technologies, Inc.

Jim Browning
Boise State University

JVST B
Journal of Vacuum Science & Technology B

ARTICLE

avs.scitation.org/journal/jvb

Particle-in-cell simulation of an industrial magnetron with electron population analysis

Cite as: J. Vac. Sci. Technol. B 39, 022201 (2021); doi: 10.1116/6.0000809
Submitted: 23 November 2020 · Accepted: 26 January 2021 ·
Published Online: 17 February 2021

Andong Yue,[1] Marcus Pearlman,[1] Mike Worthington,[2] John Cipolla,[2] and Jim Browning[1]

AFFILIATIONS

[1]Department of Electrical and Computer Engineering, Boise State University, 1910 University Drive, Boise, Idaho 83725-2075
[2]L3Harris Technologies, Inc., Williamsport, Pennsylvania 17701

ABSTRACT

Results from a particle-in-cell simulation study of L3Harris CWM-75 kW are presented; the continuous wave cooker magnetron typically operates at 18 kV, 5 A, 1900 G, 896–929 MHz. The startup process of the device has been simulated in 3D by using the PIC code VSim. The startup behavior was examined with (1) no priming, (2) RF priming, and (3) cathode modulation. Under no priming, the simulated device failed to oscillate in a simulation time of 1000 ns. Oscillations were achieved with both RF priming (150 ns) and cathode modulation (180 ns). Half (~40 kW) of the device's typical operating power at a frequency of 915 MHz, the device's π-mode frequency, was used for the RF priming, and the priming was active only during the first 50 ns of the simulation. The device then oscillated later, but oscillation soon failed as the spokes collapsed. Continuous cathode modulation was also performed at 915 MHz with stable oscillation after 180 ns. A method for analyzing the electron device physics during the magnetron startup was developed by examining time-dependent particle distribution profiles in r and φ. These results provide insight into the conditions in the electron hub that lead to oscillation, particularly the azimuthal velocity distribution where the distribution shows a clear low or negative velocity prior to the start of oscillation.

I. INTRODUCTION

Magnetrons are highly efficient, high-power microwave sources that have a wide range of applications from industrial cooking to military radar. Industrial magnetrons are free-running oscillators; while having the advantage of ultra-high efficiencies up to ~90%, they have the serious drawback of having a drifting phase.[1–3] The drifting of the output phase limits the usefulness of the device for phase-sensitive applications such as telecommunication and phase-controlled radar. This phase-drifting issue also brings power scaling challenges for the device due to its inability to work in array arrangements. A solution to this phase-drifting problem is, thus, crucial for unlocking the full potential of the device. One solution to the phase-drifting issue is injection-locking, which involves the use of an external feedback system (a reflection amplifier) that sends a signal into the output of the magnetron oscillator. Extensive work has been done on this topic by Brown.[4,5] The injection-locking approach to the phase-drifting issue has the drawback of significantly reduced device efficiency when the magnetron is controlled in this way. This work aims to explore a different approach to reach phase coherency.

Previous simulation work of a 2D Rising Sun magnetron has indicated that phase-control may be possible by modulating electron injection into the magnetron interaction space at the RF frequency to form and control the electron spokes. Our new work considers a commercially available continuous wave cooker magnetron (L3Harris CWM-75 kW) to explore the feasibility of using modulated electron injection to control the start-up and phase of the magnetron.[6–9] The following article discusses the characteristics of the CWM-75 kW magnetron, provides a description of the PIC model, and presents results from a study of the magnetron's start-up behavior and the effects of modulated electron injection. Then, a new technique to analyze the electron population is presented. The new analysis technique leverages custom codes developed in R to calculate the probability mass distributions of the electron population's positions and velocities in separate cylindrical axes. Then, the probability mass distributions are plotted against time in the form of intensity plots. These plots present ways to look at magnetron physics during the startup process and display physical behaviors that are not obvious from typical data analysis.

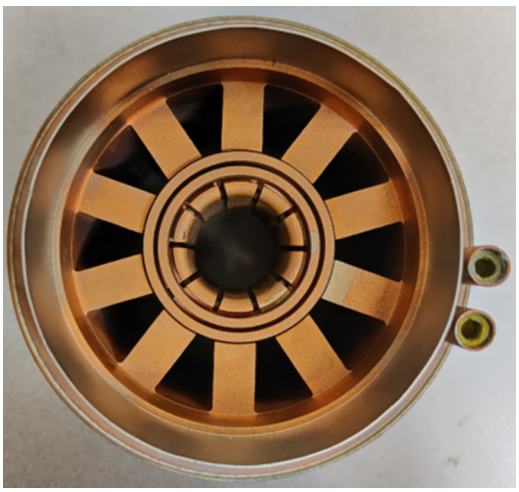

FIG. 1. Photograph of the top-down view of the circuit of L3Harris CWM-75 kW magnetron. The helical cathode structure is not shown. The circuit has an inner radius of 14.58 mm and an outer radius of 52.26 mm.

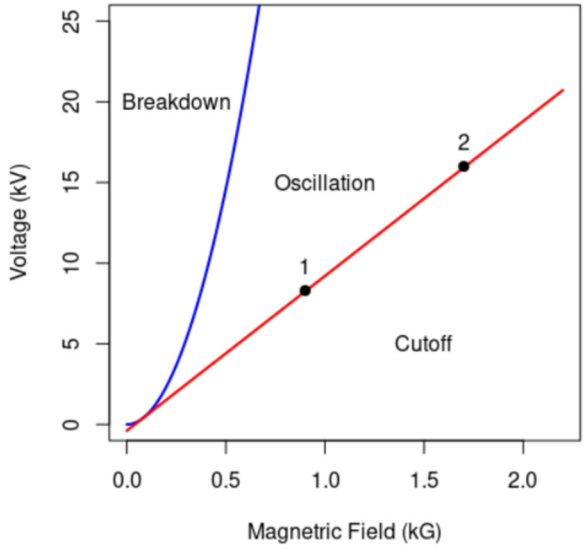

FIG. 2. Hull cutoff (blue) and Hartree condition (red) of the CWM-75 kW. 1: Typical operating point (1800 G, 18 kV), 2: low-voltage operating point (900 G, 8.3 kV).

II. BACKGROUND AND THEORY

L3Harris CWM-75 kW is a continuous-wave industrial cooker magnetron capable of 75 kW of sustained power output. A photograph of the magnetron circuit (top down) is shown in Fig. 1. In this image, the cathode is removed, and the extraction antenna is not shown. The typical operating parameters for the device are listed in Table I. The device is strapped and connections at three locations on the vanes extract the power as will be shown later. The device cathode is a helix that is 48 mm long and 12.789 mm in diameter. The circuit's inner radius is 14.58 mm, and the outer radius is 52.26 mm. There are end-hats at the top and bottom of the cathode.

In a magnetron, for any given external axial magnetic field, the DC-voltage regime that allows oscillation is bounded above by the Hull cutoff, the cutoff voltage for magnetic insulation, and is bounded below by the Buneman Hartree condition, the voltage at which the phase velocity of the slow-wave structure matches the $E \times B$ velocity of the hub electrons.[10,11] The Hull cutoff and the Buneman Hartree condition for the CWM-75 kW were calculated by using methods presented by Lovelace and Young; the results are summarized in Fig. 2.[11] For the desired π-mode at 915 MHz, the phase velocity is approximately 8.4×10^6 m/s. Two operating points are indicated in the figure. The first is the typical operating parameters of the magnetron at 18 kV and 1800 G. As is clear in the plot, the operating point lies just above the Hartree line. Hence, the electron hub just meets the condition for oscillation which results in the nearly maximum potential energy extraction from the electrons and results in the high device efficiency (~90%). Another operating point was also tested at L3Harris and is shown in Fig. 2 as point No. 2. This low power operating point is at 900 G and 8.3 kV and requires only 150 mA to oscillate. This operating point was studied for planned experiments at the Boise State University using a gated field emission cathode as proposed in prior work.[6–9] Again, the operating point is just above the Hartree line. It is worth noting here that Lau *et al.* have shown that the Brilluoin flow model extends the Buneman Hartree condition to the right of the single-particle model.[12] Although a field emission current injection model was not used in the simulation results, the use of such an injection model has been recently explored in VSim.[13] A limited parameter sweep of the DC voltage (V) and the applied magnetic field (B) was performed near the device's typical operating point; however, since the typical operating parameter was experimentally confirmed, all simulation results to be presented in the following sections use these typical operating parameters; the use of the lower power operating parameters will be studied in later research.

TABLE I. Operating parameters of the CWM-75 kW.

	Cathode voltage	Current	Magnetic field	Frequency
Typical CWM-75kW	−18 kV	4.75 A	1800 G	896–929 MHz

III. SIMULATIONS

A. Overview

Simulation studies of the magnetron were conducted by using the 3D PIC code VSim.[14] The detailed geometry of the magnetron was constructed with CAD based on measurements provided by L3Harris Technologies (as seen in Fig. 3). The scale

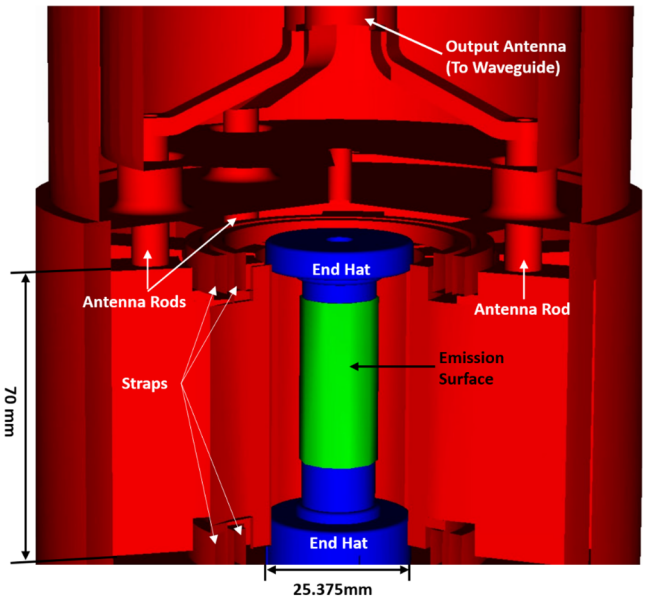

FIG. 3. Geometry model of the CWM-75 kW used in the VSim simulation. The green emission surface for the cathode is contiguous and replaces the actual helical cathode, which would be too computationally expensive to model. The blue regions represent the end-hats, and the red regions represent the copper conductor of the circuit and extraction structures. Three rods connect to vanes and these rods merge to form an antenna which sits inside a waveguide (which is not modeled).

of the simulated geometry and the physical geometry of the CWM-75 kW is 1:1, resulting in a size of 110 mm by 110 mm by 127 mm for the simulation domain, which was then uniformly subdivided into rectangular cells. The cell size was determined based on the smallest geometry in the domain, which was the 3.9 mm gap between the circuit straps. These constraints result in a cell size of 0.5 mm by 0.5 mm by 1 mm. This rather coarse simulation grid was used to keep the computational time as short as possible while adequately resolving the strap geometry. The time step size is 0.5 ps, which is compliant with the Courant–Friedrichs–Lewy (CFL) condition, and the macroparticle size is about 10^6. In the original assembly, the output antenna is embedded inside of an output waveguide, which was not included in the simulation to reduce the size of the simulation domain for shorter computational time. The loading effect of the output waveguide onto the cavity was mimicked by adjusting the setting for the upper −z simulation boundary in VSim. A 300 ns simulation takes roughly two days to compute when 16 cores of computational power are used.

A constant external magnetic field was defined over the entire simulation domain in the −z direction. The DC voltage between the anode and the cathode was achieved by defining a constant, 1-cell-thick, electric field between the anode geometry and the cathode geometry at the lower −z boundary. The upper −z boundary was defined as an open boundary to represent a perfectly matched output waveguide. Particles were emitted from the emission surface with a Richardson–Dushman emission profile,

$$J = M \times (4\pi me/h^3) \times T^2 \exp(-W/T),$$

where J is the resulting magnitude of the current density (A/m^2), M is the multiplier, m is the electron mass (kg), e is the electron charge, h is Planck's constant, T is the temperature (K), and W is given by

$$W = W_0 - (e/4\pi\epsilon_0) \times |\boldsymbol{E}f|,$$

where $\boldsymbol{E}$ is the surface electric field (V/m), f is the enhancement factor, and W_0 is the work function (eV).[14] For the simulation results to be presented, a work function (W_0) of 4.5 was selected, and the multiplier M was iteratively tuned to achieve the 4.75 A of emission current from the cathode.

Back-bombarding electrons are absorbed by the cathode, and back-bombardment current is recorded by the simulation as "cathode current." The simulation model does not take account of the effect of secondary emission.

As will be shown, the magnetron will not oscillate in a reasonable simulation time (<1000 ns) without some form of priming to start the oscillations. This is not unexpected as this magnetron typically begins oscillation in milliseconds, although it should be noted that others have shown this magnetron can start oscillation within 1000 ns in simulation under space charge limited conditions.[15,16] Several types of priming have been studied over the years including RF priming, cathode modulation priming, and magnetic field priming to initiate oscillation within PIC simulations.[6–9,17–20] Some simulations, such as the Rising Sun magnetron, can oscillate without priming.[6–9] In this work, three simulation cases are studied: no priming, RF priming, and cathode modulation priming.

B. Frequency response simulation

Before simulating the startup of the device, simulations were conducted to find out if the frequency response of the cavity was consistent with expectation. The load-free resonant frequency of

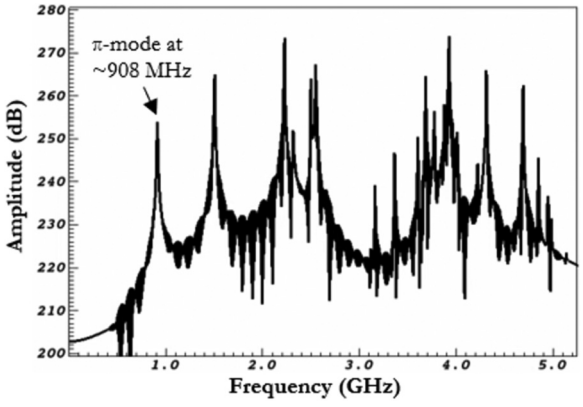

FIG. 4. Frequency response of the simulated device from 0 to 5 GHz.

the π-mode should be around 908 MHz. To simulate the frequency response of the magnetron cavity, a short (~20 ns) distributive current pulse containing multiple frequencies was defined inside of one of the magnetron resonators. This current induces fields that contain multiple frequencies, and the cavity will only resonate with frequencies that match the cavity resonance, and frequencies that do not match will be suppressed. Then, the frequency response of the cavity can be identified by extracting the frequency components of the resonate cavity voltage after steady-state has been reached. No particles or additional electric or magnetic fields other than those induced by the current pulse were used. The simulated frequency response of the cavity is shown in Fig. 4. The π-mode is at the lowest resonance frequency, which is 908 MHz according to the simulation result shown. The simulated π-mode frequency matched the known device π-mode frequency, which indicates that the simulated cavity geometry is correct.

C. Reference case: No priming

Before applying priming techniques to simulations, it is important to run a simulation without priming to establish a baseline. The simulation was run for the typical operating parameters shown in Table I. Figure 5 shows the typical result of the voltage in the resonant cavities over time; no meaningful oscillation can be observed before the simulation ended at 1000 ns. The cavity voltage is extremely low (~20 V). Figure 6 shows the 2D cross-sectional electron distribution plot at the center plane of the cavity at the end of the simulation time; it shows a ring-shaped electron hub (the dots are macroparticles) near the cathode. There is little to no interaction between electrons and the anode, which again indicates an absence of oscillation. A parameter sweep has been performed on a matrix of voltages from 15.5 to 19 kV and applied magnetic fields from 1600 to 1900 G; none of the tested parameters led to oscillation without priming. This result is consistent with the expectation that some kind of priming technique is required to start the device in a reasonable amount of simulation time.

D. Magnetron start-up with RF priming

For this simulation, a current was defined in the resonator cavities in a way that induces the π-mode. The input power of this priming was tuned to 40 kW, about half of the operating power of the magnetron. This driving current was turned on at the beginning of the simulation and was shut off after 50 ns, and then the magnetron was allowed to free run. Figure 7 shows the cross-sectional electron distribution at various time instances. At the beginning of the simulation [Fig. 7(a)], electrons are being emitted uniformly from the cathode and π-mode RF priming is active; Fig. 7(b) shows the electron distribution pattern when the RF

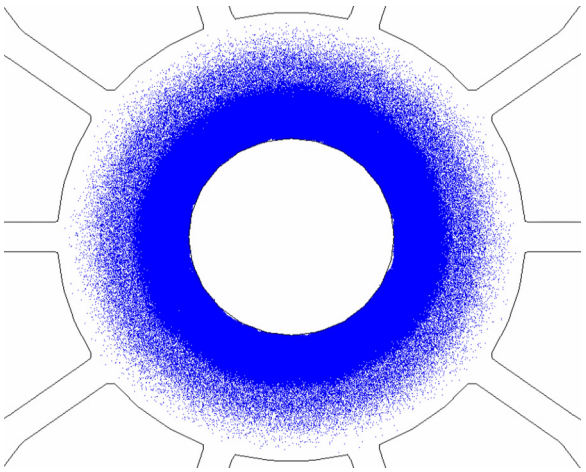

FIG. 6. 2D cross-sectional electron distribution plot from VSim at the center plane of the cavity at the end of the simulation with no priming. Blue dots represent electron macroparticles. Electrons uniformly distribute around the cathode indicating the lack of circuit interaction.

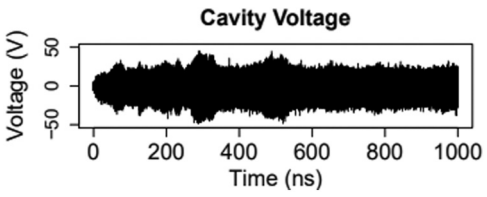

FIG. 5. Voltage in the resonant cavities over time with no priming in VSim; note that the amplitude of the voltage oscillation is minimal.

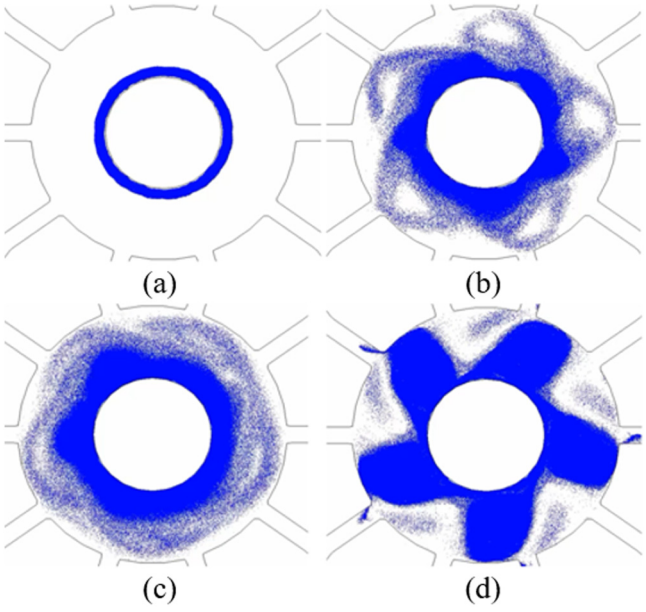

FIG. 7. Cross-sectional electron distribution with RF priming. (a) 0.5 ns, (b) 50 ns, (c) 100 ns, (d) 150 ns.

priming current shuts down (50 ns). The RF priming current creates an electric field that pulls electrons away from the cathode and forms a five-spoke π-mode pattern. This pattern gradually collapses after the RF priming current is turned off at 50 ns, as Fig. 7(c) shows that the spokes are not well-defined at 100 ns. At this point, it looks as if the device is not going to oscillate, but then the five-spoke π-mode pattern re-emerges at about 140 ns, and Fig. 7(d) shows the device begins to oscillate to full power at 150 ns.

Figure 8 shows the cavity voltage, anode and cathode currents, particle counts, and RF power versus time. After the RF priming current was turned off at 50 ns, both the cavity voltage and the power gradually decreased with the cavity voltage decaying to as low as 25% of the peak cavity voltage during priming, and the output power decaying to below 10% of the peak output power during priming; however, around the 150 ns mark, the device suddenly begins oscillation, and the output power is near the 75 kW operating power of the device. Although the RF priming current drove up the cavity voltage when it was active during the first 50 ns of the simulation, anode current remained low. Additionally, when the device begins to oscillate at 150 ns, the anode current spikes to as high as 10 A, but the cathode current did not drop to near zero, indicating strong electron back-bombardment. Also, a rapid drop in particle count was observed. This indicates the existence of "super spokes," which occurs when an unsustainably large number of electrons are absorbed by the anode in a short time-window.[6–9] Then, the oscillation broke down and does not re-emerge for the remainder of the simulation.

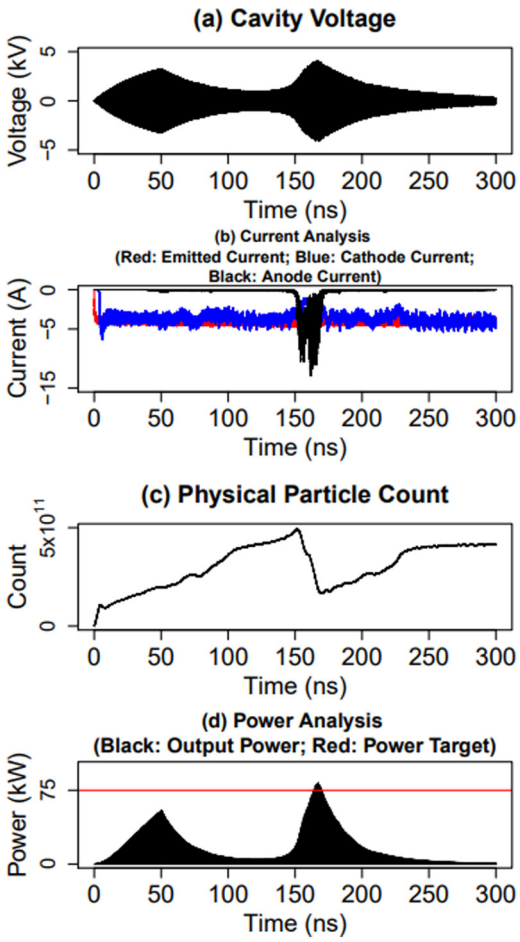

FIG. 8. VSim results for RF priming turned off at 50 ns showing (a) cavity voltage; (b) emission, anode, and cathode currents; (c) number of simulated macroparticles; (d) RF power (red line denotes the power target at 75 kW).

E. Magnetron start-up with cathode modulation

In this case, electrons were injected in five evenly spaced locations around the cathode, and these injection spots rotate around the cathode as a function of time at 915 MHz to drive the π-mode. This approach is similar to that described here.[6–9] Additionally, a ten-sided cathode was used to match the planned experimental cathode approach as also described for the previous Rising Sun research.[6–9] An experimental cathode has been developed by using low temperature cofired ceramic (LTCC) and gated field emission arrays (GFEAs).[21,22] Figure 9 shows the cross-sectional electron distribution at various time instances: (a) 0.5 ns, (b) 10 ns, (c) 100 ns, and (d) 180 ns.

In this case, the five-spoke π-mode pattern emerged right away, within 10 ns, and became more and more pronounced with time. Unlike in the RF primed case, the spokes had a steady build-up with no breakdown in the process. The results shown in Fig. 10 confirm this observation. The cavity voltage and power build-up were steady. Once oscillation begins, a spike in the anode current like that of the RF priming case was observed, which again

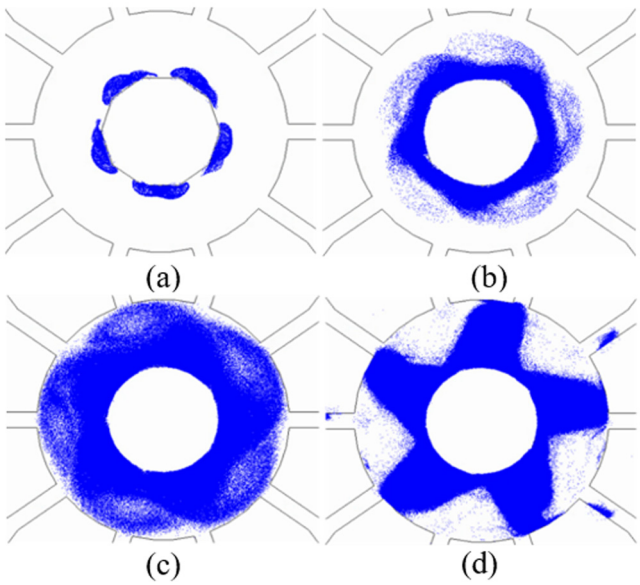

FIG. 9. Cross-sectional electron distribution under cathode priming. (a) 0.5 ns, (b) 10 ns, (c) 100 ns, (d) 180 ns.

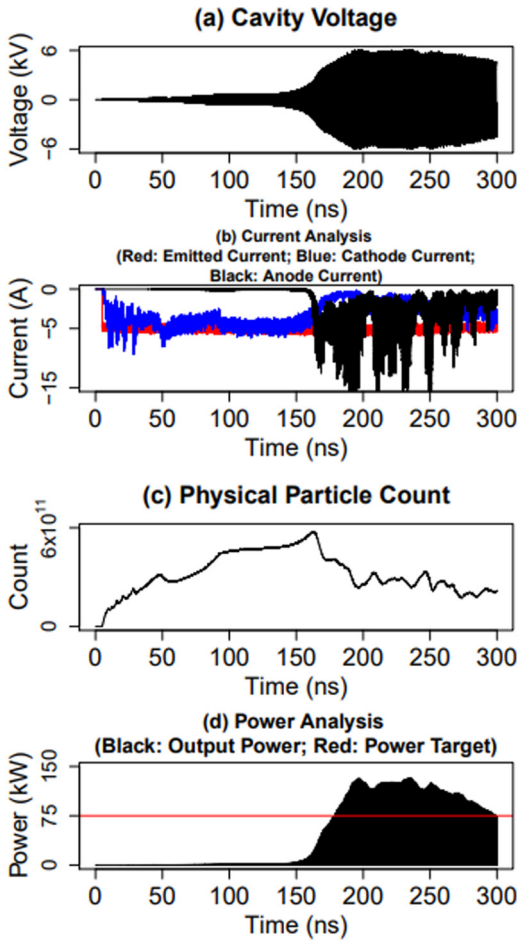

FIG. 10. VSim results for continuous cathode modulation priming showing (a) cavity voltage; (b) emission, anode, and cathode currents; (c) number of simulated macroparticles; (d) RF power (red line denotes the power target at 75 kW). Clear RF power output occurs around 160 ns.

indicates the existence of super-spokes. Nonetheless, this cathode priming case showed much better oscillation stability than the RF priming case in the sense that cavity voltage oscillation lasted much longer and did not collapse right away.

F. Comparison to prior 2D rising sun magnetron results

In the RF priming case, while the modulation eventually induced oscillation, the electron population went through a transition with spoke formation, collapse, and oscillation unlike the prior 2D Rising Sun simulations where there was continued spoke formation leading up to oscillation. In the cathode modulation case of the 3D magnetron simulation, the electron spokes did not collapse; however, unlike our prior 2D Rising Sun magnetron results, the start-up in the 3D simulation takes much longer (180 ns vs 60 ns), and the oscillation is not stable in the RF phase. Hence, while the cathode modulation technique generated magnetron start-up and led to a stable oscillation, the start-up was much slower, and there is a clear period in which oscillation appears ready to occur (40–80 ns), but oscillation appears to be stalled. Understanding the cause of this effect required consideration of the electron population.

G. Effects of the 10-sided cathode

It was observed in both the current 3D model and the prior 2D Rising Sun model that the 10-sided cathode geometry leads to better startup behavior; there were even cases when the model would only oscillate with the 10-sided cathode geometry under certain priming conditions. The issue here, however, is that the simulation grid that was used is still relatively coarse, since everything is simulated in Cartesian coordinates, curved edges are handled by the Dey–Mittra cut cell algorithms.[23] When the edges are smooth, as it is the case for the circular cathode, the cut cell algorithm seems to handle the curved surface well, but the 10-sided polygon geometry involves sharp corners, which the cut cell algorithm does not seem to resolve very well due to the discontinuity in the first and second derivatives of the geometry. Hence, although the geometry for the cathode is a 10-sided polygon, it is uncertain whether the simulation actually resolves a polygon. One potential solution is to adjust the mesh size and study its impact on the polygon geometry; another solution is to customize the simulation mesh so that all the polygon vertices are only on the mesh nodes.

IV. ELECTRON POPULATION STUDY

A. Motivation

Results from the RF primed simulation presented a curious case in which the oscillation rapidly decayed after the RF priming power was shut off at 50 ns. At 120 ns, the output power almost entirely disappeared with the output power decaying to below 10% of the priming power, and it did not appear that the magnetron was going to oscillate; however, at around 150 ns, oscillation suddenly began. On the other hand, without the 50 ns of initial RF priming, the magnetron would never oscillate within the simulation timeframe. The discrepancy in oscillation behavior between the RF primed and un-primed cases indicates that, in the RF primed simulation, some information in the electron population was retained after the initial RF priming was shut off. This result implies that attributes of the magnetron retain information that results in oscillation. Understanding this process within the magnetron could enable the magnetron to be controlled more precisely for faster startup and reduced phase drift. As mentioned above, the cathode modulation case showed strong indications that oscillation would start early, as with the 2D simulations, but the oscillation stalled. The simulation results presented above show us the results of magnetron startup physics, but they offer limited insight into that physics, so another approach was considered.

B. Device physics study

Diagnostic techniques have been developed to study the crossed-field device physics that determines the aspects of the RF

priming case, where oscillation starts well after priming stops and the start-up of the cathode modulation case in which the spokes appear to form immediately but actual oscillation is delayed. Analysis codes have been developed in the language R to extract the radial position distributions, radial velocity distributions, azimuthal position distributions, and azimuthal velocity distributions of the electrons as functions of time. The analysis that has been developed is cross-sectional. The current method analyzes all electrons within the same time instance; then, it attaches results from all time-instances together to form a complete picture. All calculations were performed within the data matrices of individual time instances; this is the reason why electron tracking across time steps was not needed for this analysis. The plots to be shown in the following section are the normalized probability mass functions of the electron distributions; darker colors indicate a higher probability of finding an electron in the corresponding position or velocity region. Radial plots use electron populations for all the azimuthal positions (0 to 2π), while azimuthal plots include electrons from all radial positions ($r_{cathode}$ to r_{anode}); all use z-data.

The analytical methods developed so far focuses on the electron data generated by VSim. For all the simulations discussed, VSim was set to dump electron data every 1000 time steps; because the time step size, Δt, is 500 fs, the electron data dumps are 0.5 ns apart. For all cases presented below, the simulations were run for 300 ns each, resulting in 600 electron data files for each case. In total, each analysis involves the processing of double precision datasets on the order of trillion-entries.

C. Reference case: No priming

Figure 11 shows the electron density results when there is no priming for radial position, radial velocity, azimuthal position, and azimuthal velocity. Note that these plots are intended to show patterns that are not obvious by simply looking at the data matrices, and the goal of the first case is to provide a reference. The plots are divided into two regions for discussion. Under this setup, the radial position plot showed that the electrons initially appear to move away from the cathode [Fig. 11(a), region 1]; however, the process quickly reversed, and the bulk of the electrons collapsed back to the cathode [Fig. 11(a), region 2]. The radial velocity plot shows a similar result; when the simulation first started, the velocity distribution diverged from the centerline, which is zero, indicating an abundance of movement in the radial direction [Fig. 11(b), region 1]; however, the velocity distribution quickly collapsed back to the zero-line, which suggests the initial activity has faded [Fig. 11(b), region 2]. In the azimuthal direction, both plots show a lack of bunching [Figs. 11(c) and 11(d), region 2]. At the current diagnostic development stage, these azimuthal position plots offer limited information due to low data resolution. These simulations were run with a 1000 dump period, which correspond to 0.5 ns; under this resolution, the azimuthal position data cannot be adequately analyzed since it has the added challenge of being cyclical. Despite its issues, the plot is still included for completeness as the contrast in the plot will indicate electron bunching. The azimuthal velocity plot shows that the azimuthal electron velocities were random and spread out, which indicates a lack of bunching.

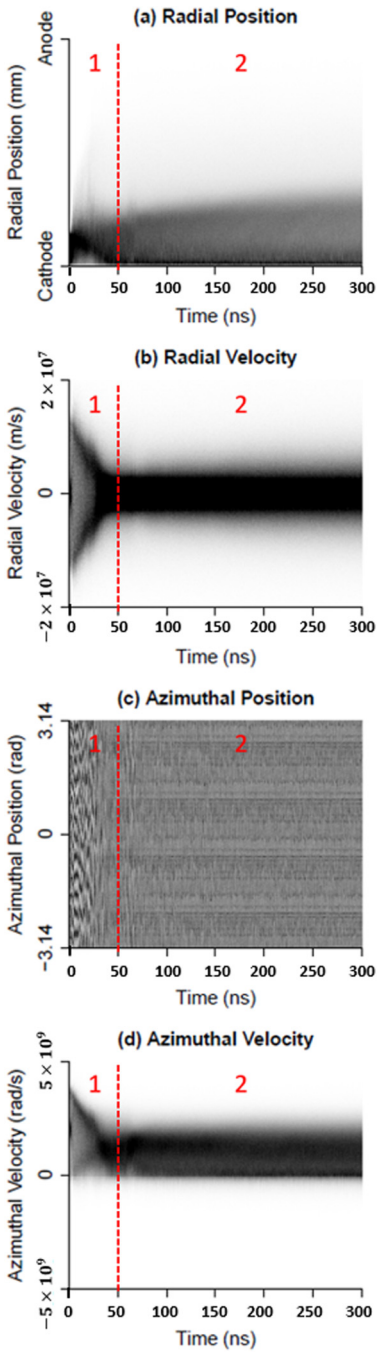

FIG. 11. Electron probability distributions as functions of time under no priming; darker color indicates higher probability. (a) Radial position, (b) radial velocity, (c) azimuthal position, (d) azimuthal velocity. At the beginning of the simulation (region 1), the radial position plot shows electrons started to cross the anode–cathode gap, but were magnetically insulated, and for the rest of the simulation (region 2), the electrons were never able to reach the anode. This is confirmed by the azimuthal position plot region 2, which shows an absence of bunching, and the velocity plots show a lack of bunching.

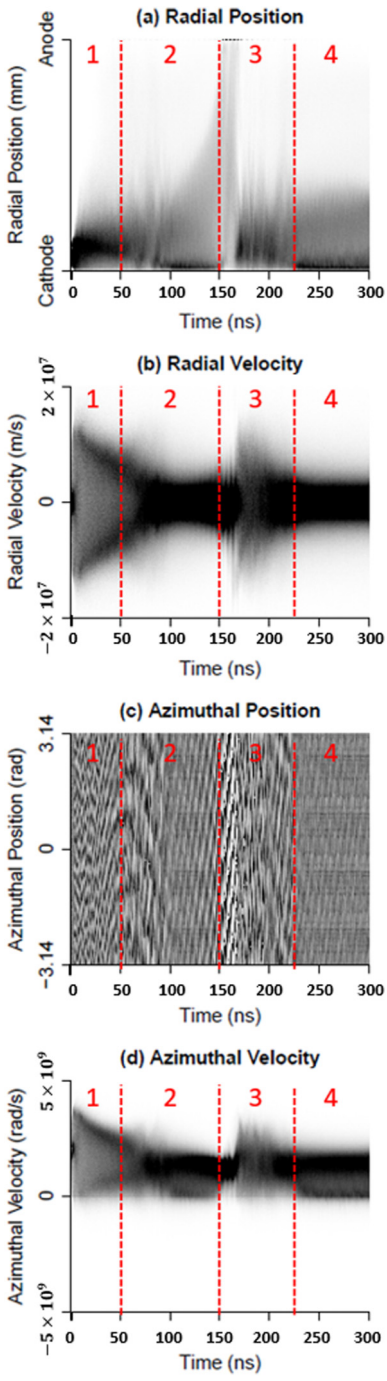

FIG. 12. Electron probability distributions as functions of time under RF priming; darker color indicates higher probability. (a) Radial position, (b) radial velocity, (c) azimuthal position, (d) azimuthal velocity. RF priming was active till 50 ns (region 1), after which the convergence of the azimuthal velocity persisted (region 2) until the device reached oscillation. Oscillation collapses within 10 ns due to rapid loss of electrons (region 3) and never reappears for the remainder of the simulation (region 4).

D. RF priming

In this case, the simulation RF priming was applied for the first 50 ns, and then the priming was shut off. The results (Fig. 12) are intriguing. Here, the plots are divided into four regions. RF priming was active until 50 ns (Fig. 12, region 1), during which time the radial position plot shows the RF priming pulling electrons toward the anode; the azimuthal position plot shows a striation pattern, which indicates electron bunching. This bunching is also confirmed by the convergence of azimuthal velocity. But, the bunching did not appear to sustain after the RF priming was shut off (Fig. 12, region 2) based on the azimuthal position plot. However, the azimuthal velocity shows that the velocity convergence continued even after the RF priming was shut off. Oscillation then occurred at 150 ns (Fig. 12, region 3) at which point the azimuthal velocity shows strong convergence, and the striation pattern can once again be seen in the azimuthal position plot; the radial position plot shows that electrons were being rapidly collected at the anode within a 10 ns window. Then the oscillation collapsed due to this rapid loss of electrons. This collapse is confirmed by the divergence in radial and azimuthal velocity. The oscillation never reoccurs for the remainder of the simulation (Fig. 12, region 4).

The device has a loaded Q of about 100. The cavity voltage should decay in tens of nanoseconds after the RF priming was shut off; however, as it can be seen from the cavity voltage plot in Fig. 8, after some initial decay, from 50 to 100 ns, the cavity voltage held at a relatively constant level from approximately 100 to 140 ns before expanding again right before oscillation. Some factors prevent further decay of the cavity voltage after 100 ns and hold it at a relatively constant level before oscillation. It appears that some aspect of electron population, possibly the azimuthal velocity distribution, allows oscillation to start at 150 ns. This speculation is based on the convergence of the azimuthal velocity distribution persisting after the RF priming was shut off at 50 ns until the device reaches oscillation at 150 ns. Striations in the azimuthal position plot also show some positional remnants clearly related to RF priming, but how these patterns describe the device operation is not yet clear. As seen in the cavity voltage plot (Fig. 8), there is still an oscillating cavity voltage long after RF priming is terminated (many RF periods); hence some part of the electron population appears to be supporting this field.

E. Cathode priming

Cathode priming was applied continuously throughout this simulation. This case (Fig. 13) showed many different patterns compared to the previous two cases. The plots are divided into four regions. In this case, there was sustained spoke formation before oscillation was finally reached. The radial position plot does not show the majority of electrons collapsing back after their initial attempts to move into the anode–cathode gap, like the previous two cases; instead, it seems that the simulated device tried to begin oscillation shortly after startup but failed (Fig. 13, regions 1 and 2), and the radial velocity collapsed, while the radial position did not (Fig. 13, region 3). Once the device began oscillating at 180 ns, the radial velocity plot shows increased and

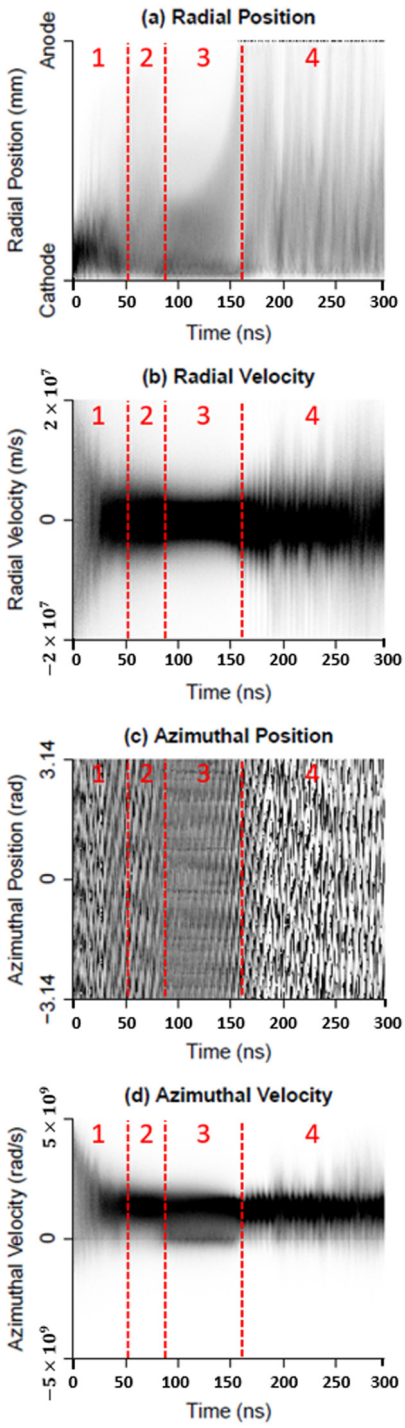

FIG. 13. Electron probability distributions as functions of time under cathode priming; darker color indicates higher probability. (a) Radial position, (b) radial velocity, (c) azimuthal position, (d) azimuthal velocity. Comparing to the RF priming case, cathode priming resulted in a better sustained electron bunching and oscillation (region 4).

then sustained activities (Fig. 13, region 4). The azimuthal position and velocity plots both indicate strong and sustained bunching after the oscillation began. The striations in the azimuthal and radial position plots are intriguing and show the transition of the magnetron from spoke formation to actual oscillation. On the other hand, the clean striation pattern in the azimuthal position only lasts for about 40 ns at the beginning of Fig. 13 (region 4) (from 150 to 190 ns); then the pattern begins to fall apart. It is likely that there are undesired modes present. Again, the device physics indicated by these results still needs to be understood as will be discussed.

F. Study of velocities

Figure 14 offers a direct comparison of the velocity (radial and azimuthal) plots across all three cases. In the no priming case, the radial velocity establishes an approximately equal magnitude of positive and negative traveling electrons as would be expected with no modulation. The priming cases show very different behavior. In cathode modulation, the electron population clearly made an early attempt to migrate toward the anode, but then the population collapsed. As indicated by the blue lines, the radial velocity plots begin to converge, and then "spikes" are seen at the beginning of oscillation for both priming cases. These spikes increase in amplitude during oscillation showing some part of the electron population is increasing in radial velocity. In the RF priming case, this effect decreases as the oscillation collapses, but in the cathode modulation case, it continues with oscillation.

The azimuthal velocity plots show a far more intriguing result. In the no priming case, after an initial increase, the azimuthal velocity drops down, and the bulk of the electrons are relatively uniform with some electrons showing an azimuthal velocity dropping near zero. However, for the modulation cases, a very clear pattern is observed just before oscillation. While again the bulk of the electrons create a tighter azimuthal velocity pattern, some electrons dip in velocity. The dip patterns in the azimuthal velocity indicate portions of the electron population are traveling slower in the azimuthal direction, which suggest these electrons' cycloidal motion have increased "hairpin" radii at the bottom of their cycloid, when the radial velocity goes to zero. In the cathode modulation case, leading up to oscillation, a portion of the azimuthal velocity even dipped deeply into the negative velocity direction, indicating a portion of the electron population is traveling counter to the direction of spoke rotation in the azimuthal direction as they form a loop at the bottom of their cycloidal motion. Then, the azimuthal velocity shows a narrowing of the velocity spread followed by clear spikes in the distribution. In both cases, the azimuthal velocity patterns show the narrowing and the transition to oscillation. The RF priming case has very large velocity excursion possibly indicating spoke collapse before returning to the same pattern as before. The cathode modulation case, in contrast, shows smaller velocity spikes and a relatively stable pattern as oscillation continues. The precise implications of these observations still require further investigation, including a better understanding of the electron kinetic versus potential energy and the electron momentum distributions.[1,11]

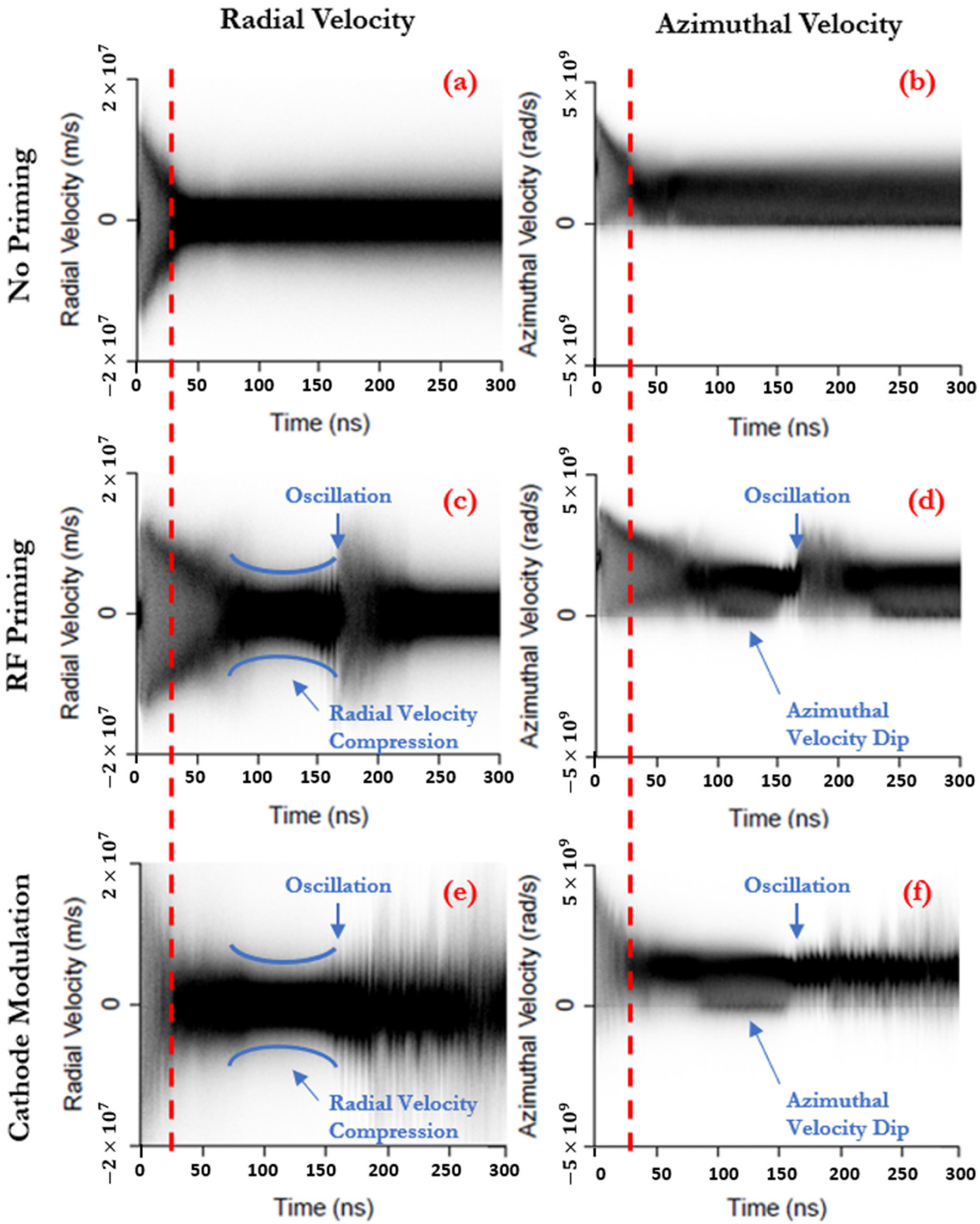

FIG. 14. Comparison of the radial and azimuthal velocities across three cases. (a) radial velocity for the no priming case, (b) azimuthal velocity for the no priming case, (c) radial velocity for the RF priming case, (d) azimuthal velocity for RF priming case, (e) radial velocity for the cathode modulation case, (f) azimuthal velocity for the cathode modulation case.

V. SUMMARY AND CONCLUSIONS

There are several conclusions from the simulation results of the three cases presented in Sec. III: (1) the RF priming case indicates the device retains some property that enabled the device to oscillate at 150 ns when the electron hub seemingly collapsed after RF priming was shut off at 50 ns; (2) the cathode modulating case suggests that cathode modulation offers better oscillation stability, at least in simulation, when compared to RF priming; (3) increased "hairpin" radii of the electron cycloidal motion and compression of the radial velocities were observed leading up to oscillation in both the RF priming case and the cathode modulation case. In both, the RF priming case and the cathode modulation case, the oscillation collapsed due to super-spokes, which caused spikes in anode current that led to rapid loss of electrons. The causes of these super-spokes are unclear at this point.

Electron population analysis codes were developed to capture and visualize the "internal information" (position distributions, velocity distributions in separate dimensions, and their combinations) that is not readily noticeable by looking at global information such as electron position and cavity voltage. The analysis for the RF priming case suggests that some aspect of start-up is stored in the azimuthal velocity since the converging pattern persisted after the RF priming was shut off. In the cathode modulation case, the disorder in the azimuthal position plot that emerged 40 ns after oscillation indicates the existence of undesired RF modes. The suppression of these undesired modes could be the key to improving the magnetron phase drift. The azimuthal velocity plots just prior to oscillation show that some electrons reach a low velocity at the bottom of cycloid orbit and even move in the opposite direction. It is unclear if this is a cause or an effect of oscillation start but could provide a method to study magnetron oscillation startup by programming the electron population. It is worth noting here that this new electron population analysis scheme, while still in the early stages of its development, has shown promise in revealing a better understanding of the electron device physics in magnetron startup. Although the analysis scheme is developed for analyzing magnetron simulation results, it might be applied to the analysis of electron populations of other vacuum electron devices and possibly plasma devices.

The next steps for this research include further improvements to the analysis method presented in Sec. IV in terms of accuracy and resolution; an improvement in resolution (particularly smaller time increments for the data dumps) is expected to reveal additional details that could lead to further understanding of the electron population during magnetron startup. The azimuthal position and velocity plots will be broken down into different radial sections in future analysis. The results presented in Sec. IV are all cross-sectional analysis in the sense that particle statistics were performed within discrete time steps. Analysis methods and codes are currently being developed to analyze the data in terms of time-series in which particles are tracked across time steps to form trajectories, and then statistics can be performed based on the particle trajectories to extract a distribution of trajectories. This new tool will further enable the study of particle trajectory behaviors within the magnetron's interaction space during startup under different priming conditions. These efforts include studies of the Slater orbits and particle trajectory autocorrelation. Of particular interest is the breakdown of electron cycloidal flow into Brillouin flow by studying the electron orbits and their effects on oscillation. The goal is to investigate what types of particle trajectory behavior create a favorable environment for the magnetron to oscillate. In addition, electron population studies have begun on the 2D Rising Sun magnetron model to take advantage of the much shorter computational times and reduced datasets of the 2D model compared to the 3D model.[6–8] New analysis codes will be first applied to the 2D model so that they can be tested and refined before being applied to the computationally intensive 3D model.

ACKNOWLEDGMENTS

The material support for this work is provided by the Air Force Office of Scientific Research under Award No. FA9550-19-1-0101. Geometry drawings and the magnetron hardware were generously provided by L3Harris Technologies. Technical support of the VSim code was provided by Tech-X Corporation. Special thanks to John Luginsland for useful discussions.

DATA AVAILABILITY

The data that support the findings of this study are available from the corresponding author upon reasonable request.

REFERENCES

[1]G. B. Collins, *Microwave Magnetrons* (McGraw-Hill, New York, 1948).
[2]J. C. Slater, *Microwave Electronics* (Van Nostrand, New York, 1950).
[3]A. S. Gilmour, Jr., *Microwave Tubes* (Artech House, Norwood, 1986).
[4]W. C. Brown, "A reporting of personal observations of noise in magnetrons and CFAs", Report R-75, Raytheon Research Division, Lexington, KY (1976).
[5]W. C. Brown, *Proceedings of the 1st International Workshop on Crossed-Field Device, Ann Arbor, 15–16 August* (University of Michigan Press, Ann Arbor, MI, 1995), Vol. 178.
[6]S. Fernandez-Gutierrez, J. Browning, M. C. Lin, D. N. Smithe, and J. Watrous, J. Appl. Phys. **119**, 044501 (2016).
[7]S. Fernandez-Gutierrez, J. Browning, M. Lin, D. N. Smith, and J. Watrous, J. Vac. Sci. Technol. B. **33**, 031203 (2015).
[8]S. Fernandez-Gutierrez, J. Browning, M. Lin, D. N. Smith, and J. Watrous, *Simulation of a Magnetron Using Discrete Modulated Current Sources* (IEEE, Washington, DC, 2014).
[9]S. Fernandez-Gutierrez, J. Browning, M. Lin, D. N. Smith, and J. Watrous, J. Vac. Sci. Technol. B **32**, 061205 (2014).
[10]J. M. Creedon, J. Appl. Phys. **48**, 1070 (1977).
[11]R. V. Lovelace and T. F. T. Young, Phys. Fluids **28**, 2450 (1985).
[12]Y. Y. Lau, J. W. Luginsland, K. L. Cartwright, W. Tang, B. Hoff, and R. M. Gilgenbach, Phys. Plasmas **17**, 033102 (2010).
[13]L. Li, K. Aranganadin, H. Y. Hsu, and M. C. Lin, J. Vac. Sci. Technol. B **38**, 023205 (2020).
[14]See https://txcorp.com/images/docs/vsim/latest/VSimReferenceManual.pdf for Richardson-Dushman Emitter (accessed 25 January 2021).
[15]A. D. Andreev and K. Hendricks, J. Microwave Power Electromag. Energy **44**, 114 (2010).
[16]A. D. Andreev and K. Hendricks, IEEE Trans. Plasma Sci. **40**, 1551 (2012).
[17]W. M. White *et al.*, IEEE Trans. Plasma Sci. **34**, 627 (2006).
[18]M. C. Jones, V. B. Neculaes, Y. Y. Lau, R. M. Gilgenbach, and W. M. White, Appl. Phys. Lett. **85**, 6332 (2004).
[19]B. W. Hoff *et al.*, IEEE Trans. Plasma Sci. **36**, 710 (2008).
[20]V. B. Neculaes *et al.*, IEEE Trans. Plasma Sci. **33**, 94 (2005).
[21]D. Black, R. Harper, P. Ward, J. Davlin, O. Bentancourt, D. Plumlee, and J. Browning, Int. J. Appl. Ceram. Tec. **17**, 2393 (2020).
[22]S. A. Guerrera and A. L. Akinwande, Nanotechnology **27**, 295302 (2016).
[23]S. Dey and R. Mittra, IEEE Microw. Guid. Wave Lett. **7**, 273 (1997).